Experiments in Fluids (2022) 63: 134
https://doi.org/10.1007/s00348-022-03487-6

RESEARCH ARTICLE

On the applicability of LDV profile-sensors for periodic open wet clutch flow scenarios

Robin Leister[1] · **Saskia Pasch**[1] · **Jochen Kriegseis**[1]

Received: 19 April 2022 / Revised: 27 June 2022 / Accepted: 26 July 2022 / Published online: 13 August 2022

Abstract

The present experimental study revolves around the applicability of a Bragg-shifted laser Doppler velocimetry profile sensor (LDV-PS) in use for open wet clutch flow scenarios, where sub-millimeter gap height and textured surfaces are present. It is shown that the LDV-PS is capable to determine angular-resolved 1D3C velocity information, with all complex flow structures, depicted properly that are present in a radial groove. For the flow measurements the sensor is tilted to ±30° compared to the axial orientation to enable the opportunity to reconstruct angular-resolved 1D3C velocity fields from two consecutively conducted runs. This facilitates measurement results with high axial and angular resolution for the complete open clutch flow and proves for the first time, that a profile sensor is capable to extract 3C information with the mentioned method. The results show that all characteristic flow structures occurring in the investigated sub-millimeter rotor-stator gap flow can be recorded properly. This insight renders the LDV-PS a promising and straight-forward applicable means to support industry-relevant research so as to uncover formerly hidden flow features and thus contribute to advanced development approaches for the respectively considered applications.

Graphical abstract

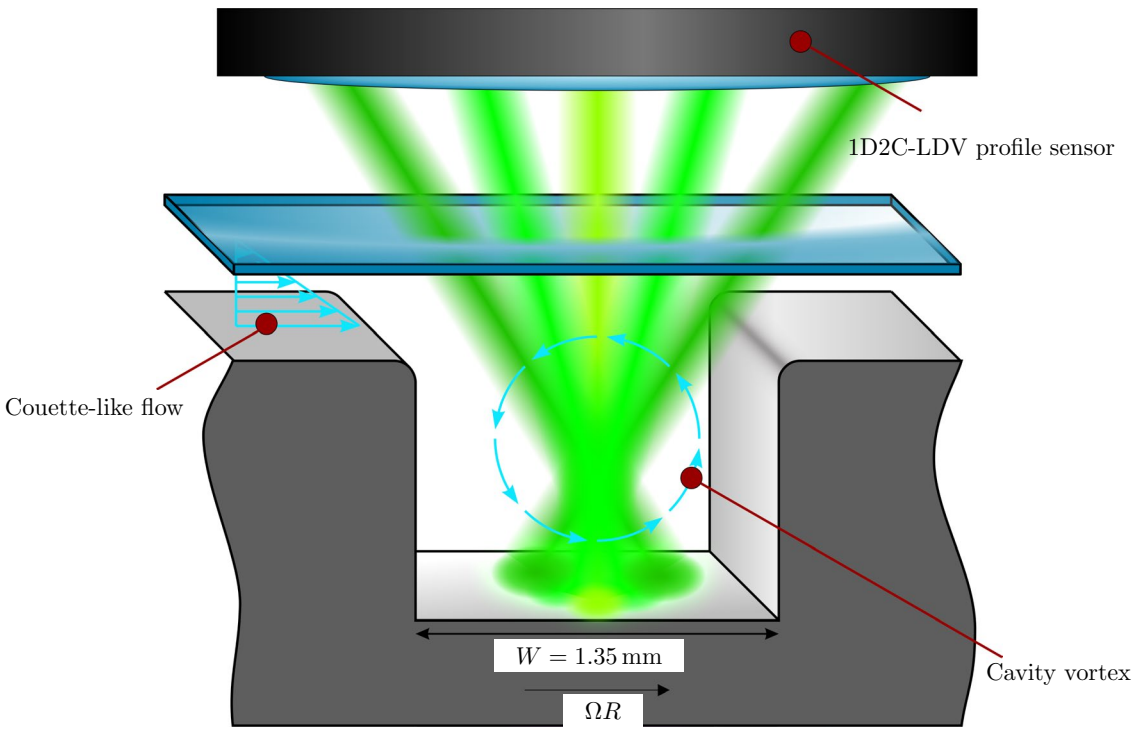

Extended author information available on the last page of the article

1 Introduction

The continuously essential demand for saving CO_2 and the expectation of an increasing range of electric drive concepts constantly push the efforts to develop new energy-saving strategies in the automotive industry. Optimization of the idling behavior of wet multi-plate clutches is one such promising strategy. The speed difference between drive and output, in combination with the presence of oil and a height of the lubrication gap in the sub-millimeter range leads to a considerably high wall shear stress, which sums up to an adverse so-called drag torque. This unfavorable quantity was first discovered in R &D departments of industrial companies, but soon was adapted from universities and research institutions, where a variety of torque-minimizing studies with numerical and experimental approaches were conducted. Among others, Pahlovy et al. (2016) formulated an analytical model and provided some visualization-based insights, while Neupert and Bartel (2019) conducted an experimental drag-torque investigation with different groove patterns. More recently, Leister et al. (2020) formulated a dimensionless approach to compare numerical, experimental and analytical results, and Groetsch et al. (2020) created a numerical approach for drag-torque calculation, which focused on speed and performance.

To optimize and manipulate the drag torque, a large multiplicity of surface-texturing groove designs such as e.g. radial, sunburst or waffle groove patterns were introduced on one disk (see Neupert et al. 2018), but no detailed distinction between different flow topologies and/or velocity-field quantification has been conducted. As such, a quantitative evaluation of the groove-pattern geometry as well as subsequent modelling and prediction efforts, as yet, largely build upon integral torque measurements. This lack of circumferentially resolved velocity-profile information across the investigated rotor-stator gaps likely stem from limited commercially available and straight-forward applicable velocimetry techniques. In addition to limited optical access to the open clutch, moreover also the strong velocity gradients, groove pattern periodicity and—in turn—required angular resolution introduce various additional side conditions during experimentation. Despite excellent spatio-temporal resolution, typical volumetric whole-field approaches such as three-dimensional particle tracking velocimetry (3D-PTV) (Nishino et al. 1989), tomographic Particle Image Velocimetry (Elsinga et al. 2006) or Shake the Box (Schanz et al. 2016), suffer from the limited optical access and sensitivity against test-rig vibrations.

One step towards more detailed flow diagnostics in such gaps was done by Leister et al. (2021), who used a single-camera defocusing particle tracking velocimetry (DPTV) as means to extract volumetric velocity information from the 540 µm gap of an open wet clutch with radially grooved rotating disk. This technique offers precise and robust velocity and shear-stress information, and is particularly suitable for this type of flow scenario. Sub-millimeter vortex structures in the groove have been detected in this DPTV study with a spatial resolution of 12 µm along the optical axis. However, missing commercially available evaluation software renders the application of DPTV difficult for R &D branches of clutch-disks manufacturer, which likewise holds true for other industry branches dealing with sub-millimeter rotor-stator gaps. Furthermore, the effect of shadowing inside the grooves and correspondingly hidden flow domains become an increasing issue when investigating more complex groove geometries.

An alternative measurement technique is the so-called Laser Doppler Velocimetry profile sensor (LDV-PS), which is considered in the present work. LDV-PS was initially introduced by Czarske (2001); Czarske et al. (2002), and then adapted and improved in the following years (see e.g. Büttner and Czarske 2003, 2006; Bayer et al. 2008). As such, this measurement technique serves as promising means for the above-outlined sub-millimeter gap-flow scenarios, which have already been indicated in a generic proof-of-concept study by Kriegseis et al. (2016) for a commercially available single-component (1C) LDV-PS. This technique was already used for some challenging other flow scenarios, such as, for instance, the flow inside a hard disk drive model (Shirai et al. 2011, 2013) or the induced velocity of magnetic gradients on electro-deposition (König et al. 2013). More recently, the LDV-PS approach has been successfully applied for industry-near projects like a fuel-cell stack by Bürkle et al. (2020). A useful extension with two detection components (2C) and a successful demonstration of a Bragg-shifted version was recently published by Burgmann et al. (2021), who successfully identified flow reversals in the wake of a droplet.

Accordingly, the major objective of this work is a detailed applicability examination of a Bragg-shifted 1D2C LDV-PS to a sub-millimeter gap flow, as it occurs in an open wet clutch. To achieve this aim, first the sensor uncertainty for the velocity region of interest is analyzed artificially by a wire of a diameter of 10 µm, which was particularly chosen to approximately mimic the size of the subsequently supplied tracer particles.

The findings of the first part prepare the ground for the gap flow measurements, where the measurement-inherent quantities are stated for this clutch flow. The main flow experiments are repeated for two different sensor angles to furthermore allow a retroactive reconstruction of a 1D3C velocity field from two consecutive 1D2C measurements, similar to earlier efforts with standard LDV measurements

(see e.g. Pashtrapanska et al. 2006). The data evaluation procedure is described and argued, where a combined velocity/location binning of the data appears as advantageous for further investigations.

The final part contains fluid mechanic findings and the processed flow measurement results as occur in an open wet clutch. A cavity vortex positioned in the radial groove is identified from the LDV-data. The evaluation is done in an angular-resolved manner and derived quantities such as wall shear stress (WSS) are derived successfully, which enables the technique as promising means for further considerations of open clutch flow measurements.

2 Experimental procedure

2.1 Measurement principle

The main difference between a profile sensor compared to a conventional LDV set-up is the use of two overlapping fringe systems with different spatial gradients, wherewith one velocity component and the position of particles passing through the measurement volume can be detected. The beam waist positions of the two laser systems are, therefore, shifted longitudinally away from the intersection point in opposite directions. Thus, the fringes are diametrically opposed and the fringe spacings $d_{\mathrm{f},i}$ for $i = 1, 2$ are a function of the x_3-position as illustrated in Fig. 1, where the complete used LDV-system is

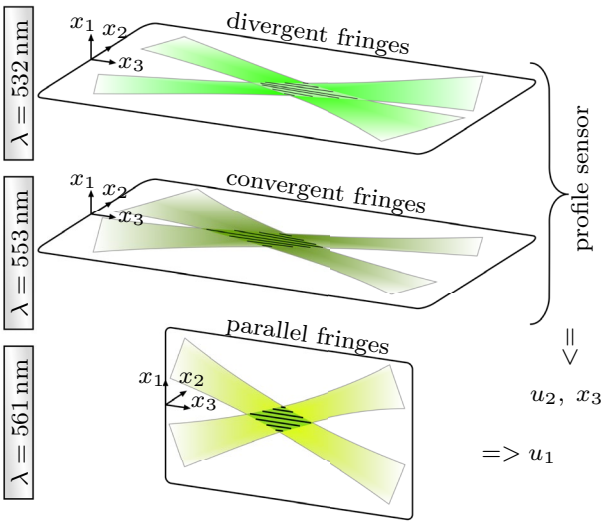

Fig. 1 Equipment of the used LDV-PS. The first two components provide one velocity component and the spacial information, the third component with parallel fringes provides a second velocity component

decomposed for the different laser beams. The x_3-position of the particles can be determined by the quotient q of the received Doppler frequencies f_{i} which is given by $q(x_3) = f_2/f_1 = d_{\mathrm{f},1}(x_3)/d_{\mathrm{f},2}(x_3)$, if the velocity u_1 is equal to u_2. x_3 can then be found by means of a calibration function. Once the x_3-position of a particle is found the local fringe spacings $d_{\mathrm{f},i}$ and the resulting velocity u can be calculated retroactively. Therefore, the calibration procedure is of major importance for the measurement process, which is normally done already by the manufacturer. According to Czarske et al. (2002) the uncertainty of the position can be stated as

$$x_3{}^{\sigma} = \sqrt{2}\frac{\partial x_3}{\partial q}\frac{f^{\sigma}}{f}. \tag{1}$$

A possible location error depends on the slope of the calibration function q and the ratio of frequency uncertainty f^{σ} and the frequency f. Possible measurement errors are a low Signal-to-Noise ratio (SNR), a undersampled burst signal or—in case of a industry-near application—vibrations of the test rig. With the newly developed Bragg-shifted version of the LDV-PS it becomes furthermore possible to detect quasi-stationary particles, as occur e.g. in recirculation bubbles (cp. Burgmann et al. 2021).

For the conducted experiments an *ILA R &D* 1D2C-LDV Profile Sensor with two Nd:YAG lasers ($\lambda = 532$ nm and $\lambda = 553$ nm) and an additional laser in a general LDV set-up ($\lambda = 561$ nm) to determine a second velocity component is employed as shown in Fig. 1. The two lasers featuring the profile sensor functionality detect the circumferential velocity and the general LDV set-up detects the radial and axial velocity. All components are Bragg-shifted with a frequency of 5 MHz (40 MHz native modulation with downsampling) and the focal length of the applied front lens of the sensor is 160 mm. Additional profile-sensor parameters are summarized in Table 1. The calibration quotient q together with the fringe distances for the used LDV sensor is depicted in Fig. 2. For the velocity measurements, the coincidence mode of the LDV-sensor was enabled, resulting in the measurement of only those particles, that were registered with all three laser components. Each channel's validation option must be met in order to lead to

Table 1 Parameters of the LDV–PS used for this study

	Laser component 1	Laser component 2
Wavelength	532 nm	553 nm
Power	150 mW	150 mW
$d_f(x_3 = 0)$	1.25 µm	1.90 µm
$\frac{\partial q}{\partial x_3}$	0.000083 1/µm	

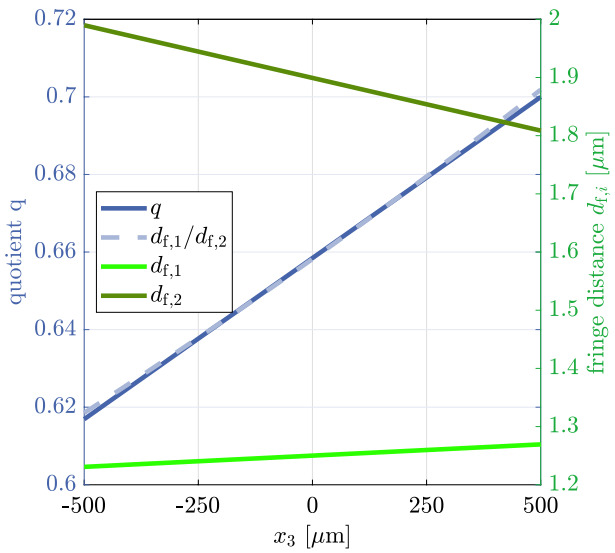

Fig. 2 The linearized calibration curve q, used for this LDV profile sensor together with the associated fringe spacings $d_{f,i}$ over x_3 for both spanned fringe patterns

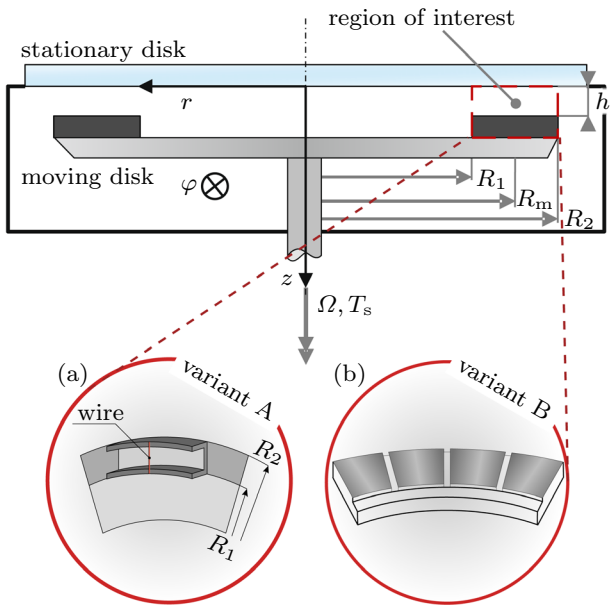

Fig. 3 Scheme of an open clutch with all relevant parameters and the region of interest for the LDV investigation and both conducted experimental set-ups; **a** wire for uncertainty conducts, **b** radial groove for flow measurement

a valid coincidence signal. Moreover, the position limit of the profile sensor (600 µm) must be satisfied.

2.2 Experimental set-up and test rig variants

The set-up for all conducted experiments is an open wet clutch facility, which comprises a single-stage rotor-stator configuration as shown in Fig. 3. The stator plate serves as optical access with anti-reflection coated float glass window to guarantee a low distortion of the inbound and scattered light. As rotating counterpart, an interchangeable disk construction serves the purpose to operate different groove patterns or non-grooved clutch plates. For a repeatable and precise movement of the rotating disk unit a *nanotec ST11018L8004* stepping motor was used. Angular-resolved measurements are enabled due to a *WL100L-F2231* light barrier sensor.

For the uncertainty quantification of the LDV-PS system the test rig is equipped with *variant A*, according to Fig. 3. A wire of diameter $d_w = 10\,\mu m$ is mounted on the rotating plate at different rotational velocities. The sensor is tilted to face the wire orthogonal and the stationary housing of the test rig with the glass plate is removed. The set-up for these studies is shown in Fig. 3(a) and aims to mimic a particle at exactly the same angular and lateral position, as well as a known and constant velocity. Similar test set-ups were conducted by Czarske et al. (2002) and are carried out during the calibration of the LDV-PS at the manufacturer. This set-up is referred to as *wire set-up* or *variant A* below.

The flow structure investigation, as actual test scenario, is progressed with a radially-grooved rotor disk and oil in between the gap of the rotor and stator, as sketched and referred to as variant B in Fig. 3. The clutch is operated at an angular velocity of $\Omega = 12.6$ 1/s, which equals a low-to-moderate circumferential disk velocity (according to Iqbal et al. 2013, for instance) and corresponds to an expected disk velocity of $u_\varphi = 1.1$ m/s at the mean radius $R_m = (R_1 + R_2)/2$. The inner and outer radii of the disk are $R_1 = 82.5$ and $R_2 = 93.75$ mm. The disk features 32 evenly distributed radial grooves with a bottom groove width of $W = 1.35$mm and height of $H = 0.97$ mm. The gap between rotor and stator is adjusted to $h = 320\,\mu m$. The measurement ellipsoid length is adjusted to 600 µm and traversed in 200 µm steps through the gap along the sensor axis. Despite full coverage of the entire gap with the ellipsiod, the traversing appears necessary, since the measuring region in z-direction spans a length of $h + H = 1.29$mm at the groove locations. The adjustments of the ellipsoid length resulted from the findings of the conducted wire experiment as will be elaborated further below. The radial position of the measurement ellipsoid for both inclination angles was located at the mean radius R_m and validated with the expected disk velocity.

The applied white mineral oil ($\rho_o = 850\,kg/m^3$, dynamic viscosity $\mu = 0.0136\,kg/ms$, refractive index $n = 1.4$) has been seeded with silver-coated hollow glass spheres ($d = 14\,\mu m$; $\rho_p = 1700\,kg/m^3$), which corresponds to a characteristic time scale of $\tau_p = 1.36 \times 10^{-6}$ s and a Stokes number of $S_k = 0.0047$, considering the gap height as characteristic

length scale. The gap and the inner part of the clutch were filled with oil to ensure a single-phase flow through the gap, but no additional external volumetric flow rate was applied. The corresponding gap Reynolds number as already discussed by Daily and Nece (1960) results in $Re_h = \Omega h^2/\nu = 0.08$. The corresponding lubrication Reynolds number is $Re_l = \Omega R_m h/\nu = 22.0$, which is considered for the present flow scenario (cp. also Leister et al. 2020).

2.3 Evaluation of the third velocity component

To extent the velocity-component measurement and also to avoid influential light reflections, the sensor is tilted forwards and backwards to an angle of $\alpha = 30°$ compared to the z-axis. The x_3-axis as indicated in Fig. 1 is rotated with $\pm 30°$ compared to the z-axis of the test rig as indicated in Fig. 4. This way of measurement enables particle detection in proximity to the disk where normally the reflected light limits the detection of the particle's Mie scattering.

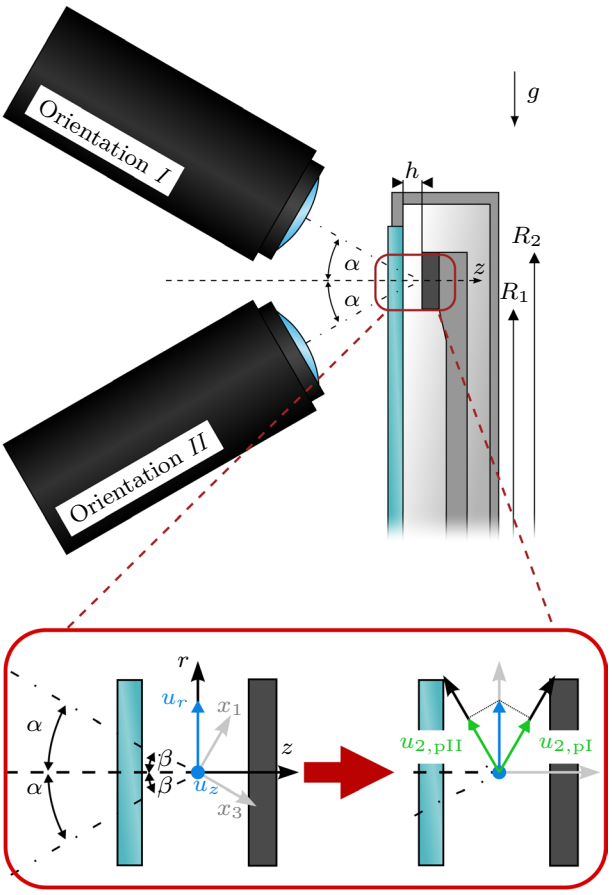

Fig. 4 LDV set-up scheme with both orientations for the LDV-PS ($\alpha = 30°$). The insert explains the conversion from the measured signal to the $\{r, \varphi, z\}$-system. The dominant u_r-component is positive (blue arrow) and the u_z-value tends towards zero (indicated as blue dot). u_φ is pointing orthogonal to the sketch plane

Additionally, this enables the retroactive determination of the third flow component, which would otherwise, be impossible to capture with an LDV sensor and this complex geometric set-up. The two considered sensor positions as used for the flow measurements are shown in Fig. 4.

While the circumferential velocity component u_φ is measured with the profile sensor lasers and directly with either sensor positions I and II, both components u_r and u_z are combined in the second conventional recorded velocity component perpendicular to the sensor axis in the $r-z$ -plane. According to the sensor orientations, this second component is referred to as $u_{2,\mathrm{pI}}$ and $u_{2,\mathrm{pII}}$, for sensor orientation *I* and *II*, respectively; see Fig. 4. The difference of $2\alpha \geq 60°$ has been recommended for the extraction of two velocity components by Morrison et al. (1991) and Orloff and Snyder (1982). A summary of the different sources contributing to error propagation is summarized by Tropea (1995). Several additional influences are caused by the test rig and the inclination of the sensor. These circumstances lead to a change in the interference pattern for all components. The calibration curve as shown in Fig. 2 could not be directly applied to the output z-position but some systematic deviation must be corrected to reach meaningful results. The main sources of deviation are summarized in the following. First, the glass plate leads to a shift of the actual sensor position in comparison to a purely geometric consideration as e.g. outlined by Shirai et al. (2008). Second, the refractive index of the oil (and the glass plate) leads to an angular deviation, which must be addressed accordingly via a calculation with the law of refraction. The z-position of each detected particle is thus corrected. Additionally, the velocity information is transformed and corrected.

Table 2 shows the measured and calculated velocity components for clarity. The detected velocities of the second component can be divided into the radial and axial velocity according to

$$u_{2,\mathrm{pI}} = \cos\beta\, u_r + \sin\beta\, u_z \tag{2a}$$

$$u_{2,\mathrm{pII}} = \cos\beta\, u_r - \sin\beta\, u_z. \tag{2b}$$

As such, the measured velocities of each particle can be split into the radial and axial velocity component, which are then expressed as:

Table 2 Orientation of the LDV-PS system against the z-axis to measure and/or determine the velocity components u_φ, u_r and u_z at the desired perimeter

Orient	Angle	Meas. quantities	Calc. quantities
I	30°	u_φ and $u_{2,\mathrm{pI}}$	u_r and u_z
II	−30°	u_φ and $u_{2,\mathrm{pII}}$	u_r and u_z

$$u_r = \frac{u_{2,\mathrm{p\,I}} + u_{2,\mathrm{p\,II}}}{2\cos\beta} \tag{3a}$$

$$u_z = \frac{u_{2,\mathrm{p\,I}} - u_{2,\mathrm{p\,II}}}{2\sin\beta}. \tag{3b}$$

Note that the refractive-index matched angle $\beta = \arcsin(\sin\alpha/n)$ is applied in (2) and (3) to account for the fluid properties of the chosen oil.

Equation set (3) directly emphasizes the interplay between the consecutively recorded data sets, where any possible error comprised in the results from either sensor orientation, can immediately affect both determined velocity components u_r and u_z. Consequently, the quality of both calculated velocity components relies on both measured orientations.

The conversion from (2) to (3) is illustrated in the insert of Fig. 4, which displays the smooth part of the gap without grooves for clarity.

3 Results

3.1 Uncertainty considerations for velocity, space and angle

For the spatial uncertainty study the mentioned $d_w = 10\,\mu\mathrm{m}$ wire and *variant A* of the set-up was used; see Fig. 3(a). The uncertainty of z-direction is directly linked to the profile sensor function, while the φ-coordinate is allocated to the recorded LDV signals from the timing unit of the encoder.

For this experiment, the sample rate was fixed at 50 MHz and the signal window was set to 8K. The higher velocities could have been sampled with a smaller signal window, however, all velocities are present in the gap flow, so fixed values for these quantities fulfill the applicational requirements. A more precise detection for the low velocities would be easily manageable with further extension of the sample rate and the signal window for each specific velocity range.

Figure 5 shows all detections of the wire for five different velocities and their calculated spatial locations. A clear trend to increasingly scattered location estimation is observed for lower velocities. Table 3 shows this variation of the results in terms of the standard deviation σ. Approximately 1500 wire detections have been recorded for each velocity to ensure statistical significance of the data evaluation process. Possible sources for the occurring scatter are a low signal-to-noise ratio of the light signal caused by strong reflections within the sub-millimeter gap; an unadjusted signal window for low velocities, which leads to an undersampled frequency signal and vibrations caused by the test rig in this slightly rough industry-related scenario. The uncertainty

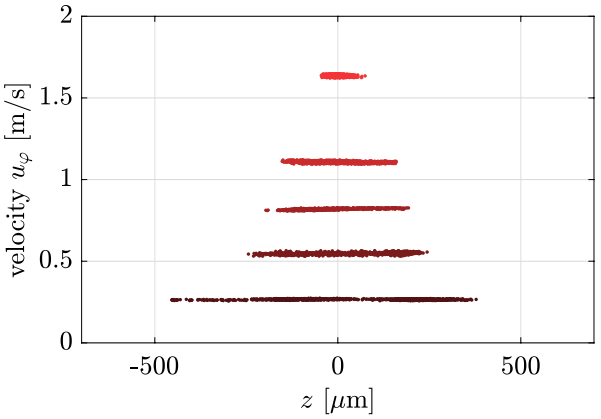

Fig. 5 All measured wire velocities and positions for a constant record length. Higher velocities meet the expected spatial uncertainty, lower velocities reveal more location estimation scatter, thus requiring a broader sample size

Table 3 All measured wire velocities with corresponding standard deviations of location and velocity

Velocity u_φ [m/s]	z^σ [µm]	${u_\varphi}^\sigma$ [m/s]
0.27	185	0.0042
0.55	129	0.0042
0.82	82	0.0046
1.11	80	0.0059
1.64	19	0.0057

can be systematically diminished with a high number of overall detections in the low velocity regime, which will be considered for the flow measurements. As a result of the above insight—the measurements of the fluid flow have been partitioned into measurement ellipsoid lengths of 600 µm, as already indicated in the previous section, thus matching every velocity range with suitable parameters. This partially compensates for the high uncertainty for low velocities.

An additional determination strategy arises from the scattered data of Fig. 5 in terms of possible averaging methods. In principle averaging in space or velocity is possible, where either the determination of the velocity statistics can be performed for a given spatial binning of the data, or—vice versa—the location statistics can be determined for preset velocity bins. For low velocities definitively an average over certain velocity bins make sense since this quantity varies much less compared to the spatial distribution. Additionally, a velocity averaging doesn't coop with this strong change in uncertainty, which improves the averaging results in general. Averaging in space appears suitable when the velocity is high enough and the possible arising error can be considered as small enough for the examined flow. For more complex flows and flows with a non-injective functional space-velocity relationship (e.g. local maxima/

minima) more elaborated evaluation strategies appear suitable. Particularly, the application of fitting functions and/or advanced averaging methods, which e.g. combine velocity and spatial averaging relative to the occurring gradients, can be envisioned. In the present context, the flow in the groove reveals a local velocity maximum slightly higher than the rotational velocity of the disk and thus only a weakly-pronounced gradient in z-direction, as further elaborated below. Consequently, a 4th-order polynomial has been chosen to approximate the velocity distribution.

Since the spatial location is the most crucial quantity is discussed sufficiently, the following part focuses on all velocity and spatial components that were conducted with *variant A* of the set-up and are essential for the considered flow scenario. Figure 6 shows multiple histograms of all extracted results for a nominal angular velocity of $\Omega = 12.57$ 1/s in detail. To compare the possible errors and their propagation, the standard deviation of the stepping motor was specified by the variation of the light barrier signal, which was additionally fed into the LDV software. The mean frequency and corresponding standard deviation results in $f_m = 1.9951 \pm 0.00015$ Hz, which corresponds to a standard-deviation contribution of $u^{\sigma}_{\varphi,\,SM} = 0.000083$ m/s of the stepper-motor variation within the u_φ-histogram.

As shown in Fig. 6(a) and (b) the circumferential and radial velocities were detected with low uncertainties, as

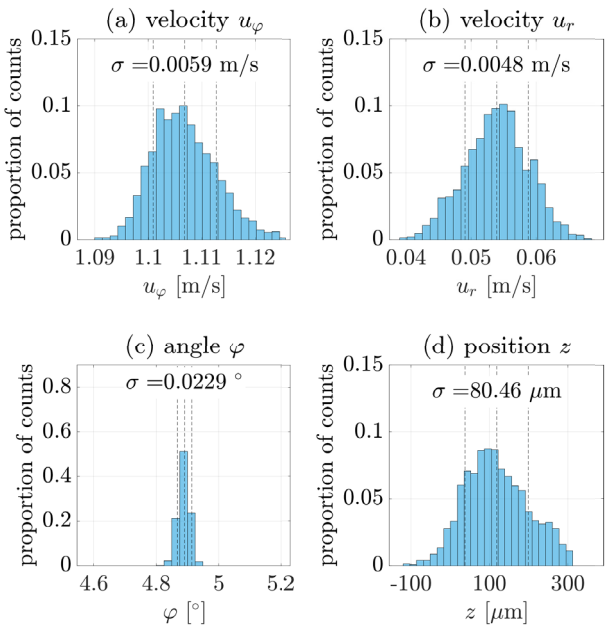

Fig. 6 Proportion of counts for the most important quantities received for the wire experiment (diameter $d_w = 10$ µm, nominal angular velocity $\Omega = \partial\varphi/\partial t = 12.57$ 1/s, radial position on the disk $R_m = 88.1$ mm). **a** circumferential velocity u_φ; **b** radial velocity u_r; **c** circumferential angle φ; **d** spatial position z within the gap

expected for LDV systems. Although the u_φ-component features the *profile sensor* function with four partial laser beams, the velocity uncertainty is within the same range as for the u_r velocity, which is provided by a classical LDV system (cp. Fig. 1). An expected higher velocity in the groove of 5% compared to the disk velocity, as uncovered by Leister et al. (2021), equals a $\Delta u_{\varphi,\mathrm{OS}}$ of 0.055 m/s in this flow scenario, which is around 10 times higher then the standard deviation. In conclusion this quantity of clutch flow pivotal element is expected to be resolved accordingly even for fairly low disk velocities which were chosen in this study.

Figure 6(c) presents the uncertainty distribution of the phase angle φ. Here only six different values with a difference of $\Delta\varphi_{\mathrm{theo}} = 0.029°$ of the 10 µm wire have been distinguished, which renders a possible theoretical uncertainty of $\Delta\varphi_{\mathrm{theo}} R_m = 44.6$ µm. Compared to the groove width W as characteristic length scale in circumferential direction the relative uncertainty is $\Delta\varphi_{\mathrm{theo}} R_m / W = 0.033$. Hence, approximately 30 different positions can be distinguished within the groove, which leads to a sufficient resolution for the given flow scenario.

The constant z-position of the 10 µm diameter wire has been detected with a standard deviation of $z^\sigma = 80.46$ µm at a wire velocity of 1.11m/s; see Fig. 6(d). This measure indicates only limited uncertainty, when compared to the gap height of $h = 320$ µm as characteristic length scale in z-direction. The relative uncertainty of $z^\sigma/h = 80.46$ µm/320 µm = 25% for the 1300 registered burst from the wire, emphasizes the necessity to further evaluate the required sample number. For the given problem, a relative uncertainty of 5% is considered sufficiently accurate, which corresponds to an absolute error of 16.0 µm. Consequently, more than 97 individual measurements are required assuming a Gaussian error distribution.

3.2 Clutch flow measurements

Figure 7 shows the detected particles (blue dots) in a $z - u_\varphi$ -diagram for $\varphi \in [7°, 11.25°]$, corresponding to a smooth region of the disk sufficiently displaced from the groove. The dashed black line shows a linear profile for comparison. The revealed linear Couette-like velocity profile is characteristic of the smooth regions of the clutch gap at low rotational velocities as elaborated by Lance and Rogers (1962), for instance. Moreover, the superimposed red bullets show the respective standard deviation z^σ of the location estimations from the wire experiment for the tested velocities, as summarized in Table 3.

Figure 8 provides an overview of the detected particles and determined quantities within one of the 32 groove-to-groove sections. Particularly, the spatial distribution across the section is shown in Fig. 8(a) in a normalized $\varphi - z$ coordinate system for all particles. The physical dimensions of

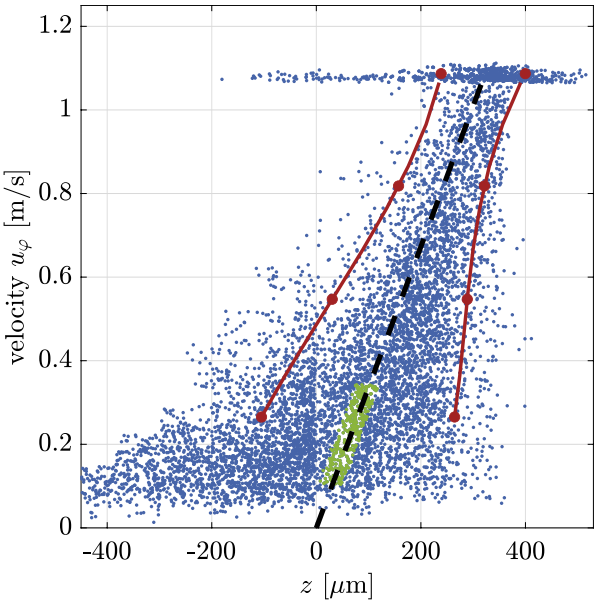

Fig. 7 Velocity component u_φ and z-position of all detected particles of the flow measurements in the smooth part of the gap flow (•) superimposed to the standard deviation z^σ for different velocities u_φ of the conducted wire experiment (•) . The green particles (•) indicate the region, which is considered for the wall shear stress measurements in Sect. 3.3

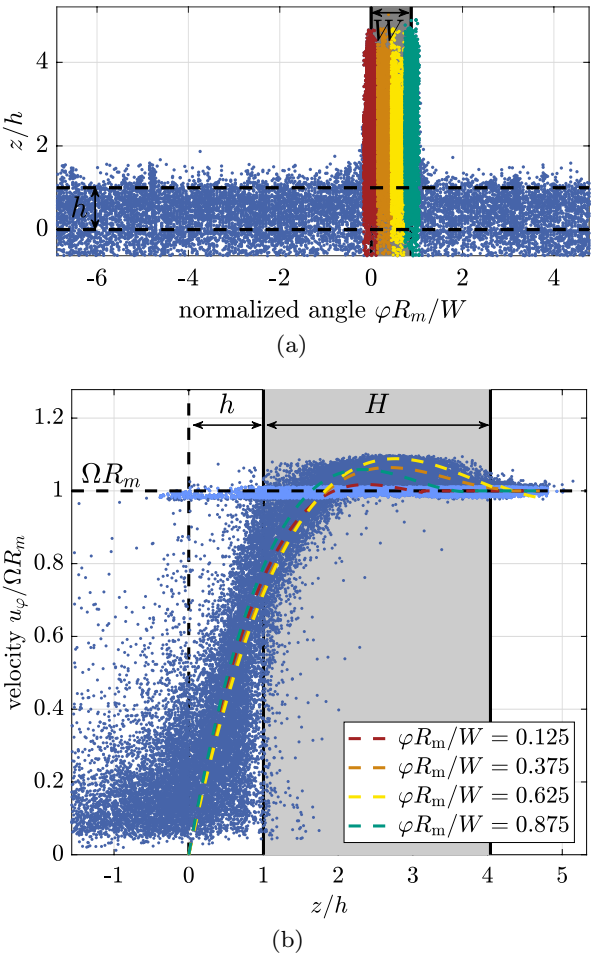

Fig. 8 (•) Registered particles across circumference and in the gap region; **a** particle locations for one section $\varphi = 7° - 18.25°$. The particles in the groove are color-coded and the dimensions W (groove width) and h (gap height) are added for comparison. The dashed lines show $z/h = 0$ and $z/h = 1$. **b** $u_\varphi(z)$ velocity profile for all registered particles within the groove section and fitted profiles for the four color-coded slices of Fig. 8(a). Additionally added: groove width W, groove height H, gap height h and the dashed line at ΩR_m. (•) Detections originating from the rotor are excluded for further calculations

the gap and the groove are illustrated for clarity. The φ-coordinate can be resolved sufficiently precise so that the start and end of the groove, namely $\varphi R_m/W = 0$ and $\varphi R_m/W = 1$, can be located. The origin of the φ-coordinate is set to the left side of the groove and normalized with R_m/W, for further clarity. In addition, the detected particles in the groove region appear color-coded along the φ-coordinate, to distinguish different slices of the flow for further (color-coded) evaluation of the averaged velocity profiles.

Particle velocities and locations across the gap and in the groove are shown in Fig. 8(b) in a normalized $z - u_\varphi$ coordinate system, which comprises particles from both the smooth and the grooved parts. As before, the rotor velocity of ΩR_m can be identified in the diagram such that particles within this small velocity band were excluded for subsequent average-velocity calculations. The particle distributions demonstrate that the velocity in the groove region is well below ΩR_m at the gap-groove interface and then advances beyond the rotor velocity well inside the groove cavity. This intra-groove vortex system has already been identified by Leister et al. (2021) and was referred to as *cavity roller*. The corresponding velocity field becomes particularly obvious from the color-coded angular-averaged velocity profiles inside the groove.

The mean velocities arise from a fitting function of higher order, which originates at (0, 0). A simple piece-wise averaging would lead to a inaccurate representation of the flow, so a more complex combination seems suitable for this flow scenario.

Figure 9 provides a comprehensive flow-field overview of all three velocity components for the selected groove-to-groove section in a normalized $\varphi - z$ coordinate system, showing each velocity component separately as contours. For visual purposes only one periodic section of the 360° -distribution with 32 grooves is shown. The circumferential velocity component is shown in Fig. 9(a) and reveals a *Couette-like* flow in nearly the complete gap. This insight is valuable information for clutch manufacturers, which up-to-now was missing in the literature. The findings now substantiate existing clutch flow models with experimental data (cp. e.g.

Iqbal et al. 2013b). Interestingly, the *Couette-like* distribution is only disturbed in vicinity of the groove. A reasonable approach for further in-detail studies might therefore focus on the region in the range of one groove width W up- and downstream of the groove (i.e. $\varphi R_\mathrm{m}/W \in [-1, 2]$) for the influence of radial grooves.

An additional aspect of the flow-structure investigation is the slightly higher circumferential velocity in the groove compared to the disk velocity. This region belongs to the above-mentioned occurrence of the cavity roller, which results from the fact that the radial groove of the present investigation is oriented perpendicular to the shear-flow direction in the gap. The cavity vortex is not limited to the groove but expands into the gap. In accordance with earlier observations by Leister et al. (2021) the highest circumferential velocity can be found in the groove's rear part and has a value of 6% above ΩR_m. As a counterpart of a higher velocity at the groove's bottom, fluid with lower velocity than ΩR_m expands into the anterior part of the groove (cp. color-coded profiles in Fig. 8(b)).

The conversion of the second recorded component u_2 from two consecutive measurements into radial and axial velocity components u_r and u_z via equation set (3) has been successfully applied, such that either component can be evaluated separately. The angular-resolved radial velocity component is shown in Fig. 9(b). The values are located in the range of 0 and 0.04 ΩR_m, with values of the smooth gap region in the lower range. The velocity at the rotor and stator tends towards zero, while the values in the middle of the gap show slightly higher velocities. This finding supports the fact that a radial outflow is present due to moderate centrifugal forces of the rotor, which for the given parameters counteracts the flow induced by gravitational forces. Additional valuable information is the higher radial outflow velocity in the groove, which is about twice as high than the smooth-gap counterpart. The highest values of around 3–4% of the disk velocity can be found in the posterior part of the groove. This is in consistency with the centrifugal forces since also the highest values of circumferential velocity are detected in this part. The findings support the fact that the radial flux is mainly dominated by the flow in vicinity of the groove and should be focused on predominantly for aeration predictions of open wet clutches.

Finally, Fig. 9(c) reveals the axial component, as likewise calculated from the equation set (2). The determined velocities largely range around zero in the smooth part of the gap. As for the groove region, however, clear patches of non-zero velocity can be identified, which are comparable in magnitude to the observed circumferential velocity deviations from ΩR_m inside the groove. These maxima are indeed mandatory to fulfill continuity of the cavity vortex. The highest velocity is located on the left side of the groove, which indicates a clockwise rotation of the cavity roller in the diagram.

3.3 Wall-shear stress determination

The potential benefit lies in the angular resolved manner of the LDV-PS, so that the influence of the respective groove patterns and correspondingly occurring flow patterns can be quantified along the entire circumference. To evaluate this footprint on the resulting drag torque, only the circumferential component is to be considered for the wall shear stress (WSS, τ_w) calculations, which leads to

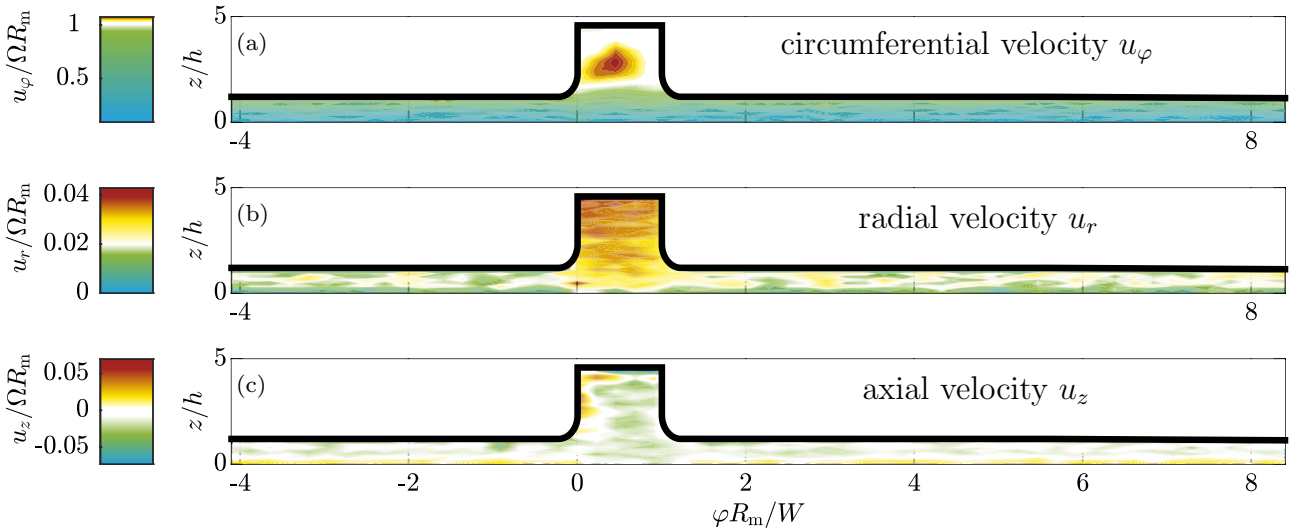

Fig. 9 Overview of the selected flow field. Contours in a $\varphi - z$ coordinate system of normalized circumferential, radial and axial velocity components, namely u_φ, u_r, u_z

$$\tau_{\mathrm{w}} = \mu \left. \frac{\partial u_{\varphi}}{\partial z} \right|_{z=0} \tag{4}$$

for the given rotor-stator shear flow. The idealized linear Couette-flow assumption in fact is an oversimplification that can be applied for very low rotational velocity components and small gap heights, as already elaborated by Daily and Nece (1960) and recently confirmed experimentally by Leister et al. (2021) for the given clutch flow scenario. Even though an ideal rotational Couette flow, consequently, is not present in this gap flow scenario—neither in the smooth part, nor the groove—the linearized profile nonetheless serves as reference, which is defined as

$$\tau_{\mathrm{w,lin}} = \mu \frac{\Omega R_{\mathrm{m}}}{h}. \tag{5}$$

To account for the mildly non-linear character of the velocity profile while maintaining a robust estimate for the WSS, a linear fit of the circumferential velocity u_{φ} in proximity of the stator in the range $z \in [70;100]\,\mu\mathrm{m}$ has been chosen for the determination of τ_{w}. Since the velocity is low in this region and the scatter around the mean velocity is accordingly strong compared to higher velocities, a direct extraction of the WSS might be heavily biased by location-estimation outliers; see Fig. 7. To overcome this issue, the standard deviation, as occurs for higher velocities, has been chosen as robust filter margin around the linear Couette approximation, to eliminate these outliers from velocity fluctuations. Consequently, the data were filtered with a validation margin of $\pm 19\,\mu\mathrm{m}$ in z-direction compared to $\tau_{\mathrm{w,lin}}$, to avoid a biased result. Figure 7 shows this region visualised with green data points for an easier comprehension. The extracted data points are binned to $\varphi R_{\mathrm{m}}/W = 0.5$ sections. Despite good overall angular resolution of $\Delta\varphi = 0.029°$ and preserved full resolution over the disk revolution, this binning appears rather coarse in comparison with the groove width W. Consequently, the formerly hidden complete groove-to-groove picture of WSS comes at the price of (circumferentially) low-pass filtered extraction of intra-groove structures and resulting variations of WSS in terms of accordingly diminished $\partial\tau_{\mathrm{w}}/\partial\varphi$ resolutions.

Figure 10 shows the extracted normalised and angular-resolved WSS τ_{w}. In accordance with earlier findings by Leister et al. (2021) the WSS values are found to be around 3% on average below the linearized $\tau_{\mathrm{w,lin}}$ in the smooth region of the gap, far enough from the groove. Assuming a constant value in this part the uncertainty of the WSS yields $\sigma = 1.29\%$, which—due to the lack of an additional reference experiment—can only serve as an estimate. Despite the relatively high uncertainty the higher value in the region of the groove can be resolved accordingly. The values are found to be 2% above the reference value of $\tau_{\mathrm{w}}/\tau_{\mathrm{w,lin}} = 1$, which—even though circumferentially low-pass filtered—preserves the observed trends from Leister et al. (2021). The highest value appears on the left side of the groove, which confirms the above-stated recommendation to consider the up- and downstream proximity of the groove in the range $\varphi R_{\mathrm{m}}/W \in [-1, 2]$ to study the influence of radial grooves on the WSS and, thus, the impact on overall drag torque.

4 Conclusions

The present study elaborates uncertainty and straightforward applicability of an angular-resolved and Bragg-shifted laser-Doppler velocimetry profile sensor (LDV-PS) for shear-flow measurements in sub-millimeter rotor-stator gaps using the example of open wet clutches with a radial groove geometry.

Initial uncertainty tests of the profile sensor with a wire of comparable size to the chosen tracer particles indicated similar velocity estimation accuracies as general LDV- setups. The location-estimation uncertainty revealed a standard deviation in z-direction of 19 µm at 1.6 m/s. For the data processing of particles with very slow velocities it turned out that a determination of location estimates for individual velocity bins outperforms the velocity estimation for spatial bins. This result gives rise to the more general recommendation that advanced data processing of LDV-PS results might also include both scatter margin and slope of the registered particles in a combined velocity/location-oriented approach. The application of such hybrid approaches requires caution since smaller flow structures might be erased from the resulting velocity profiles if unknown functional space-velocity relationships are contained in the data.

In the present setup, a ±30° angle of the sensor orientation was chosen to minimize reflection issues at the rotor,

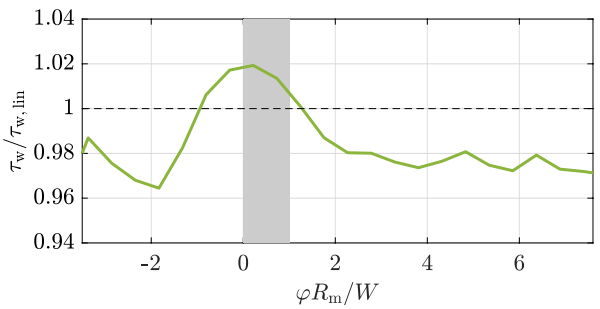

Fig. 10 Angular resolved wall shear stress (WSS) distribution (——) . The WSS for the smooth part of the gap is around 3% lower, compared to the WSS of an ideal linear profile (– –). The WSS in the vicinity of the groove (■) is significantly higher, due to the edge and the cavity roller

which moreover allowed a successful reconstruction of all three velocity components in the gap and inside the grooves. Similar approaches have been reported for standard 2C LDV application and have successfully demonstrated for the first time in the LDV-PS context along the recorded shear flow data. This insight is valuable information beyond the presented clutch-flow scenario, since it generally outlines the possibility of a retroactive conversion of consecutively conducted 2C1D experiments into angular resolved 3C1D information—given the two measurement-ellipsoid orientations remain in the same topological patterns. However, it has also to be pointed out that precise angular sensor adjustments and particularly careful experimentation is of utmost importance for an accurate determination of the axial velocity component.

The resulting flow maps for all three velocity components reveal the flow topology in the gap and the revolving grooves along the rotor circumference, which is mainly comprised of a Couette-like shear flow in the gap and cavity roller forming superimposed to significant radial fluxes in the radially oriented grooves. Since the particles have been detected with an uncertainty of 0.029°—corresponding to 44.6 µm for this flow scenario—30 different spatial positions in the groove can be distinguished in circumferential direction. This resolution provides confidence for accurate topology analyses by means of LDV-PS for more complex clutch geometries. Moreover, this circumferential resolution allows the sufficiently accurate determination of angular-resolved WSS for open wet clutches. The influence of the groove has been identified to span the limited normalized range of $\varphi r/W \in [-1, 2]$, which in turn might also serve as practical guideline for similar experimental efforts.

Even though reasonable in context of the present experiment, the angular resolution is an additional source of uncertainty, which—depending on the temporal character of the periodic signal—might increase the uncertainty of temporal derivations. This uncertainty is independent of any LDV-PS-related uncertainty limitations regarding velocity and/or location, but nonetheless might be crucial for the success of the respectively tackled problem. As such, it is strongly recommended to identify the shortest characteristic time scale and adjust angular resolution accordingly, prior to terminate experimentation of the given problem.

As a final remark, the results of this study clearly emphasize the suitability of LDV-PS as a candidate technique for industry-relevant flow-diagnostics applications. Moreover, due to the fact of an angular-resolved detection, the LDV-PS measurement technique serves as highly-suitable means to uncover the global picture of the flow topology and moreover track the WSS across the circumference. In cases, where higher spatial resolution is required, the LDV-PS results might be supplemented with inherently more precise techniques, such as defocusing particle tracking velocimetry (DPTV), for instance. Complementary application of both LDV-PS and DPTV is, therefore, considered as a landmark combination to provide substantial additional value for open clutch flow scenarios and moreover rotor-stator gap flows in general.

Funding Open Access funding enabled and organized by Projekt DEAL.

Declarations

Conflict of interest The authors declare that they have no conflict of interest.

References

Bayer C, Shirai K, Büttner L, Czarske J (2008) Measurement of acceleration and multiple velocity components using a laser Doppler velocity profile sensor. Meas Sci Technol 19(5):055401. https://doi.org/10.1088/0957-0233/19/5/055401

Burgmann S, Dues M, Barwari B, Steinbock J, Büttner L, Czarske J, Janoske U (2021) Flow measurements in the wake of an adhering and oscillating droplet using laser-Doppler velocity profile sensor. Exp Fluids. https://doi.org/10.1007/s00348-021-03148-0

Bürkle F, Moyon F, Feierabend L, Wartmann J, Heinzel A, Czarske J, Büttner L (2020) Investigation and equalisation of the flow distribution in a fuel cell stack. J Power Sources 448(227):546. https://doi.org/10.1016/j.jpowsour.2019.227546

Büttner L, Czarske J (2003) Spatial resolving laser Doppler velocity profile sensor using slightly tilted fringe systems and phase evaluation. Meas Sci Technol 14(12):2111–2120. https://doi.org/10.1088/0957-0233/14/12/010

Büttner L, Czarske J (2006) Determination of the axial velocity component by a laser-Doppler velocity profile sensor. J Opt Soc Am A 23(2):444–454. https://doi.org/10.1364/JOSAA.23.000444

Czarske J (2001) Laser Doppler velocity profile sensor using a chromatic coding. Meas Sci Technol 12(1):52–57. https://doi.org/10.1088/0957-0233/12/1/306

Czarske J, Büttner L, Razik T, Müller H (2002) Boundary layer velocity measurements by a laser Doppler profile sensor with micrometre spatial resolution. Measurement Science and Technology 13(12): 1979, http://stacks.iop.org/0957-0233/13/i=12/a=324

Daily J, Nece RE (1960) Chamber dimension effects on induced flow and frictional resistance of enclosed rotating disks. J Basic Eng 82:217–230. https://doi.org/10.1115/1.3662532

Elsinga G, Scarano F, Wieneke B, van Oudheusden B (2006) Double-frame 3D-PTV using a tomographic predictor. Exp Fluids 41(6):933–947. https://doi.org/10.1007/s00348-006-0212-z

Groetsch D, Niedenthal R, Voelkel K, Pflaum H, Stahl K (2020) Volume of Fluid vs. Cavitation CFD-Models to Calculate Drag Torque in Multi-Plate Clutches. In: WCX SAE World Congress Experience, SAE International, https://doi.org/10.4271/2020-01-0495

Iqbal S, Al-Bender F, Pluymers B, Desmet W (2013) Experimental characterization of drag torque in open multi-disks wet clutches. SAE Int J Fuels Lubr 6(3):894–906. https://doi.org/10.4271/2013-01-9073

Iqbal S, Al-Bender F, Pluymers B, Desmet W (2013) Model for predicting drag torque in open multi-disks wet clutches. J Fluids Eng 136(2):021103. https://doi.org/10.1115/1.4025650

Kriegseis J, Mattern P, Dues M (2016) Combined planar PIV and LDA Profile-Sensor measurements in a rotor-stator disk configuration. 18th International symposium on the application of laser and imaging techniques to fluid mechanics, Lisbon, Portugal, http://ltces.dem.ist.utl.pt/lxlaser/lxlaser2016/finalworks2016/papers/01.11_3_268paper.pdf

König J, Tschulik K, Büttner L, Uhlemann M, Czarske J (2013) Analysis of the electrolyte convection inside the concentration boundary layer during structured electrodeposition of copper in high magnetic gradient fields. Anal Chem 85(6):3087–3094. https://doi.org/10.1021/ac302601t

Lance GN, Rogers MH (1962) The axially symmetric flow of a viscous fluid between two infinite rotating disk. Proceedings of the Royal Society of London Series A, Mathematical and Physical Sciences 266(1324):109–121, http://www.jstor.org/stable/2414223

Leister R, Najafi A, Gatti D, Kriegseis J, Frohnapfel B (2020) Non-dimensional characteristics of open wet clutches for advanced drag torque and aeration predictions. Tribol Int 152(106):442. https://doi.org/10.1016/j.triboint.2020.106442

Leister R, Fuchs T, Mattern P, Kriegseis J (2021) Flow-structure identification in a radially grooved open wet clutch by means of defocusing particle tracking velocimetry. Exp Fluids 62:29. https://doi.org/10.1007/s00348-020-03116-0

Morrison G, Johnson M, Swan D, Deotte R (1991) Advantages of orthogonal and non-orthogonal three-dimensional anemometer systems. Flow Meas Instrum 2(2):89–97

Neupert T, Bartel D (2019) High-resolution 3D CFD multiphase simulation of the flow and the drag torque of wet clutch discs considering free surfaces. Tribol Int 129:283–296. https://doi.org/10.1016/j.triboint.2018.08.031

Neupert T, Benke E, Bartel D (2018) Parameter study on the influence of a radial groove design on the drag torque of wet clutch discs in comparison with analytical models. Tribol Int 119:809–821

Nishino N, Kasagi N, Hirata M (1989) Three-dimensional particle tracking velocimetry based on automated digital image processing. J Fluids Eng 111(4):384–391. https://doi.org/10.1115/1.3243657

Orloff KL, Snyder PK (1982) Laser Doppler anemometer measurements using nonorthogonal velocity components: error estimates. Appl Opt 21(2):339–344

Pahlovy SA, Mahmud SF, Kubota M, Ogawa M, Takakura N (2016) Prediction of drag torque in a disengaged wet clutch of automatic transmission by analytical modeling. Tribol Online 11(2):121–129. https://doi.org/10.2474/trol.11.121

Pashtrapanska M, Jovanović J, Lienhart H, Durst F (2006) Turbulence measurements in a swirling pipe flow. Exp Fluids 41(5):813. https://doi.org/10.1007/s00348-006-0206-x

Schanz D, Gesemann S, Schröder A (2016) Shake-The-Box: Lagrangian particle tracking at high particle image densities. Exp Fluids 57(5):70. https://doi.org/10.1007/s00348-016-2157-1

Shirai K, Bayer C, Voigt A, Pfister T, Büttner L, Czarske J (2008) Near-wall measurements of turbulence statistics in a fully developed channel flow with a novel laser doppler velocity profile sensor. Eur J Mech B/Fluids 27(5):567–578. https://doi.org/10.1016/j.euromechflu.2007.12.001

Shirai K, Yaguchi Y, Büttner L, Czarske J, Obi S (2011) Highly spatially resolving laser Doppler velocity measurements of the tip clearance flow inside a hard disk drive model. Exp Fluids 50(3):573–586. https://doi.org/10.1007/s00348-010-0959-0

Shirai K, Büttner L, Obi S, Czarske J (2013) An experimental study on the flow behavior near the read-and-write arm in a hard disk drive model with a shroud opening. Microsyst Technol 19(9):1519–1527. https://doi.org/10.1007/s00542-013-1847-3

Tropea C (1995) Laser Doppler anemometry: recent developments and future challenges. Meas Sci Technol 6(6):605–619. https://doi.org/10.1088/0957-0233/6/6/001

Authors and Affiliations

Robin Leister[1] · Saskia Pasch[1] · Jochen Kriegseis[1]

✉ Robin Leister
robin.leister@kit.edu

[1] Institute of Fluid Mechanics (ISTM), Karlsruhe Institute of Technology (KIT), Kaiserstr. 10, 76131 Karlsruhe, Germany